PAPER

Check for updates

Ternary transition metal Co-Fe-Ni sulfide as a high-performance anode in microbial fuel cells

Qilin Guo,[ac] Jianchun Ma,[d] Wenbo Lu, [ID][ac] Ying Wang, [ID][ac] Ergui Luo,[ac] He Xiao, [ID][ac] Li Zhang,[ac] Haishun Wu,*[ac] Tianjun Hu [ID] *[bc] and Jianfeng Jia [ID] *[abc]

The development of high-performance anode materials remains a critical challenge in advancing microbial fuel cells (MFCs). In this work, we present a novel strategy employing ternary transition metal Co-Fe-Ni sulfides to overcome the inherent trade-off between catalytic activity and structural stability commonly observed in conventional polymetallic sulfides. Through a facile one-pot solvothermal approach, we synthesized low-crystallinity $CoFeNiS_x$ (Co-Fe-Ni) ternary sulfides with precisely tunable Co/Fe/Ni molar ratios. When integrated as an MFC anode, the optimized Co-Fe-Ni sulfide delivered a maximum power density of 3915 mW m^{-2} using *Escherichia coli* (*E. coli*) as the biocatalyst, representing an 8.4% enhancement over its binary $CoFeS_x$ (Co-Fe) analogue. This performance exceeds that of most previously reported carbon-based anodes. The synthesized transition metal sulfides combine ease of fabrication with outstanding electrocatalytic efficiency. Our findings highlight the underexplored potential of ternary transition metal sulfides in engineering next-generation bioelectrochemical interfaces.

1. Introduction

With the increasing consumption of fossil fuels on Earth,[1–5] non renewable energy sources are becoming increasingly scarce,[6–8] leading to environmental problems and resource shortages.[9–12] The burning of fossil fuels results in issues such as atmospheric degradation, aquatic contamination, and a host of other ecological perturbations.[13–16] Therefore, exploring sustainable energy alternatives is crucial for solving energy shortage and environmental problems. Microbial fuel cells (MFCs) as a green, environmentally friendly, and renewable energy technology,[17–19] hold significant promise for wastewater treatment and energy recovery.[20–23] They offer an effective solution to the dual challenges of water contamination and energy scarcity, providing valuable opportunities for both social and industrial development. With the ongoing advancement of MFC technology, these systems have attracted widespread attention due to their potential to generate electricity while simultaneously treating wastewater, effectively achieving a dual benefit. This dual functionality makes MFCs particularly appealing within the realm of renewable energy production. However, despite their great potential, the widespread application of MFCs is hindered by several critical challenges.[24–29] One of the primary limitations

is low power density, which restricts their overall efficiency and scalability. Additionally, issues such as poor biocompatibility and low electron transfer efficiency at the anode surface further impede the development of MFCs.[30]

Excellent anode materials are characterized by superior conductivity, high porosity, a large active surface area, good biocompatibility, and strong stability.[31] Researchers have explored various strategies to enhance the performance of MFCs, including structural modifications, doping, and the incorporation of carbon-based materials. For example, innovative biocompatible electrodes with significant porosity and expansive surface areas have been developed to improve extracellular electron transfer within MFCs. Chao *et al.*[32,33] reported that modifying anode materials can significantly boost the power density of MFCs. Similarly, Jin *et al.*[34] demonstrated that incorporating three-dimensional carbon materials into anodes enhances microorganism attachment, thereby improving MFCs performance. Material doping has emerged as another effective strategy. Tang *et al.*[35,36] developed a three-dimensional iron-embedded nitrogen-doped carbon skeleton catalyst, significantly increasing power density and operational stability. Similarly, Ren *et al.*[37] demonstrated that introducing metal elements into biocompatible anode materials enhances electron transfer efficiency and alters material structure, facilitating the attachment of electrogenic microorganisms and improving biocompatibility. Studies consistently highlight that increasing the surface area of anode materials promotes microorganism adhesion, which improves electron transfer efficiency across the solid/liquid interface.[38,39]

Recent advances in high-entropy materials (HEMs) have revealed their exceptional catalytic properties arising from

[a]School of Chemistry and Chemical Engineering of Shanxi Normal University, Taiyuan 030031, China. E-mail: hutj@sxnu.edu.cn

[b]Shanxi University of Electronic Science and Technology, Linfen 041000, China

[c]Shanxi Center of Technology Innovation for Advanced Power Battery Material, Shanxi Normal University, Taiyuan, 030031, China

[d]Department of Chemistry and Chemical Engineering, Lvliang University, Lishi 033001, China

multi-elemental synergy. HEMs are typically defined as solid solutions comprising five or more principal elements in near-equimolar ratios,[40,41] where the high configurational entropy stabilizes the crystal structure and induces lattice distortion, leading to unique electronic properties and enhanced catalytic activity.[42,43] However, the practical application of high-entropy sulfides (HEMS, typically ≥5 elements) in bioelectrochemical systems faces inherent challenges… Medium-entropy metal sulfides (MEMS, 3–4 elements) present an attractive alternative by balancing entropy-driven stability and synthesis feasibility. Crucially, the moderate elemental complexity of MEMS allows deliberate crystallinity tuning a critical yet overlooked factor determining both electrochemical activity and microbial biocompatibility.[44] Despite their potential, there is a lack of studies examining the influence of medium-entropy sulfides on improving anode materials and their impact on the power density performance of MFCs. Further exploration of MEMS could unlock new opportunities for advancing MFCs technology and addressing current limitations in energy recovery and wastewater treatment.

In this study, a series of Co-Fe-Ni anodes with different Co/Fe/Ni compositions were prepared *via* a facile one-step hydrothermal synthesis approach. The incorporation of Ni into the Co-Fe anode material significantly enhanced both the electrochemical performance of MFCs compared to the undoped Co-Fe material. The optimized Co-Fe-Ni anode achieved the highest power output, surpassing that of the undoped Co-Fe material. Notably, Ni doping resulted in an 8.4% increase in power density. This performance enhancement is attributed to the formation of novel chemical linkages among the metallic elements introduced by the doping process, which facilitated faster electrochemical reaction rates and reduced charge transfer resistance. These findings highlight metal incorporation as an effective method for boosting the electrochemical performance of MFCs.

2. Experimental section

2.1 Preparation of Co-Fe

For the synthesis of Co-Fe, 2.4 mmol of $CoCl_2 \cdot 6H_2O$ (Aladdin) and 0.6 mmol of $FeCl_3 \cdot 6H_2O$ (Macklin) were dissolved in 50 mL of ethylene glycol (Aladdin) and heated to 80 °C under stirring for one hour. Following this, 4 mmol of thiourea (Kermel) was added to the mixture, and the solution was then agitated for another hour. Add carbon cloth (CC, 3 cm × 4 cm) to the mixed solution and sonicate for 1 hour. The resulting suspension was poured into a 100 mL autoclave. The solvothermal process was conducted at 200 °C for 12 hours within an oven. Then, the product was dried in a vacuum oven at 80 °C for a duration of 6 h, yielding the final Co-Fe (4 : 1) material.[45] Specifically, $CoCl_2 \cdot 6H_2O$, $FeCl_3 \cdot 6H_2O$, and $NiCl_2 \cdot 6H_2O$ (Sinopharm Chemical Reagent Co., Ltd) were employed as cobalt, iron, and nickel sources, respectively. Using the synthesis method described above, CoS and CoFeNi sulfides (Co-Fe-Ni) with varying Co/Fe/Ni ratios were successfully prepared. Thiourea acts as both the sulfur source and a chelating agent for metal ions, which

facilitates their attachment to the carbon cloth and enables the *in situ* growth of electrode materials.[46,47]

2.2 Material characterization

The crystallographic phases of the Co-Fe sample were conducted by X-ray diffraction (XRD) with Cu Kα radiation (Rigaku Ultima IV-185), where the scan rate is 10°/min. The sample's microstructure was investigated with a scanning electron microscope (SEM, JEOL JSM-7500F, Japan), which included an X-ray energy dispersive spectroscope (EDS). Additionally, a transmission electron microscope (TEM, JEOL JEM-F200, Japan) was employed for further morphological analysis. The oxidation states of Fe, Co, Ni, and S were determined through X-ray Photoelectron Spectroscopy (XPS, Thermo Fisher Scientific K-Alpha+ instrument) and X-ray absorption fine structure (XAFS, RapidXAFS 2M).

2.3 MFCs construction and operation

The MFC reactor employed in this work is identical to the one used in our prior study, as displayed in Fig. S1.[48] The anode was constructed from CC with Co-Fe catalyst, while the cathode was made of CC (Fig. S2), with both electrodes having an area of 1 cm^2 (1 cm × 1 cm). Each chamber held 80 mL of solution, with the anodic chamber containing 20 mL of bacterial culture. The MFCs were managed at 37 °C, and the anodic electrolyte is a phosphate-buffered saline (PBS) solution with 5.0 g L^{-1} yeast extract, 10.0 g L^{-1} glucose and 5 mM HNQ. HNQ was used as a soluble mediator to enhance electron transfer in the solution.[49] The biocatalyst in anodic electrolyte is *Escherichia coli* (*E. coli*, Fig. S3). The PBS contained 0.1 M KCl and 70 mM $K_3[Fe(CN)_6]$ were used as catholyte.

Electrochemical performance was assessed using a data acquisition system (NI 6009, National Instruments) to measure the output current and voltage. To create anaerobic conditions, the anode chamber was purged with nitrogen gas. Additional electrochemical characterization was carried out using a electrochemical workstation (CHI 660E). Linear sweep voltammetry (LSV) curves for the Co-Fe and Co-Fe-Ni anodes were carried out from 0 V to the open-circuit potential (OCP) with a scan rate of 10 mV s^{-1}. Power density values originated from the LSV data using P=UI. Electrochemical impedance spectroscopy (EIS) of complete MFC was carried out under open-circuit conditions, spanning frequencies from 10^5 to 10^{-2} Hz, with a 5 mV perturbation amplitude.[48,50] Cyclic voltammetry (CV) measurements were performed with a rate of 100 mV s^{-1} using a standard three-electrode system, where platinum foil acted as the counter electrode and an Ag/AgCl electrode served as the reference. The catalyst-loaded electrode was used as the working electrode. Tests were conducted in both PBS and the anolyte containing *E. coli*.

3. Results and discussion

3.1 Characterization of materials

Before the hydrothermal reaction, the raw material solution and carbon cloth (CC) were subjected to ultrasonic treatment,

enabling the effective fabrication of CoS, Co-Fe, and Co-Fe-Ni anode materials through a one-step hydrothermal synthesis method. As illustrated in Fig. 1 and S4, the Co-Fe, Co-Fe-Ni, and CoS anode materials were successfully synthesized using this method. The SEM images in Fig. 1a, b and S4 reveal that CoS exhibits nanoparticles attached to the carbon cloth fibers, while the Co-Fe sample consists of nanoparticle assembled into wrinkled sheet-like structures irregularly coated on the fibers. In contrast, the introduction of Ni leads to a notable morphological change, facilitating the formation of larger spherical micro-agglomerates (Fig. 1c). These agglomerates, while maintaining a particulate foundation at a finer scale, represent a distinct and more organized secondary structure compared to the binary sulfides. This evolution in morphology suggests that Ni doping significantly influences the nucleation and growth kinetics during the solvothermal process. The selected area electron diffraction (SAED) pattern in Fig. 1d shows a ring for Co-Fe-Ni, indicating the absence of a well-defined crystalline structure. High-resolution imaging in Fig. 1e confirms this, as no distinct lattice stripes are observed, further supporting the conclusion that Co-Fe-Ni possesses low crystallinity.

To investigate the element distribution in the Co-Fe-Ni sample, the corresponding energy-dispersive X-ray spectroscopy (EDS) mapping images for Co, Fe, Ni, and S are shown in Fig. 1g–k. These images confirm that Co, Fe, and Ni are uniformly distributed throughout the material, indicating that the material has a composite sulfide structure. Notably, the incorporation of Ni into Co-Fe results in a morphology change from flake-like structures to spherical particles, which is distinctly different from the Co-Fe morphology. EDS analysis

(Fig. S4) further verifies the existence of Co, Fe, Ni, and S in the Co-Fe-Ni composite.

The crystal structure of Co-Fe-Ni was analysed using XRD, as shown in Fig. 2a. The diffraction peaks for the synthesized Co-Fe material fall within the 2θ spectrum from 10° to 80°. In addition to the characteristic peaks of the carbon cloth, the XRD pattern of the Co-Fe-Ni sample shows discernible diffraction features that can be assigned to the $CoS_{1.097}$ phase, the peaks at 30.9°, 35.55°, 47.01° and 54.61° could be assigned to (204), (220), (306) and (330) planes of $CoS_{1.097}$ consisted with the JCPDS no:19-0366, respectively. No characteristic diffraction peaks corresponding to Fe or Ni species were observed, the absence of detectable characteristic peaks is likely attributable to the low crystallinity of the Co-Fe-Ni sulfide material, surfaces of low-crystallinity materials facilitate electron transfer.[51,52] The combined evidence from Fig. 1(d) and (e), along with these results, provides additional confirmation of the low crystalline order in the Co-Fe-Ni compounds. The XPS spectra of Co-Fe-Ni and Co-Fe in Fig. 2b–e and S5 show obvious signals for Co, Fe, Ni, and S. The high-resolution Co 2p spectrum of Co-Fe-Ni (Fig. 2b) reveals two pairs of Co $2p_{3/2}$ and Co $2p_{1/2}$ peaks, accompanied by two satellite peaks. The peaks at 778.4 eV and 793.7 eV correspond to Co $2p_{3/2}$ and Co $2p_{1/2}$, respectively. In Fig. 2c, the peaks at 711.9 eV and 724.3 eV correspond to Fe $2p_{3/2}$ and Fe $2p_{1/2}$,[53] indicating successful doping of Fe in the Co-Fe-Ni structure. The peaks at 855.9 eV and 874.1 eV correspond to Ni $2p_{3/2}$ and Ni $2p_{1/2}$.[54] In Table S3, the percentage of Co/Fe in different valence states was obtained through spectral fitting. Comparative analysis reveals that upon the introduction of Ni, the proportion of higher oxidation states for both Fe and
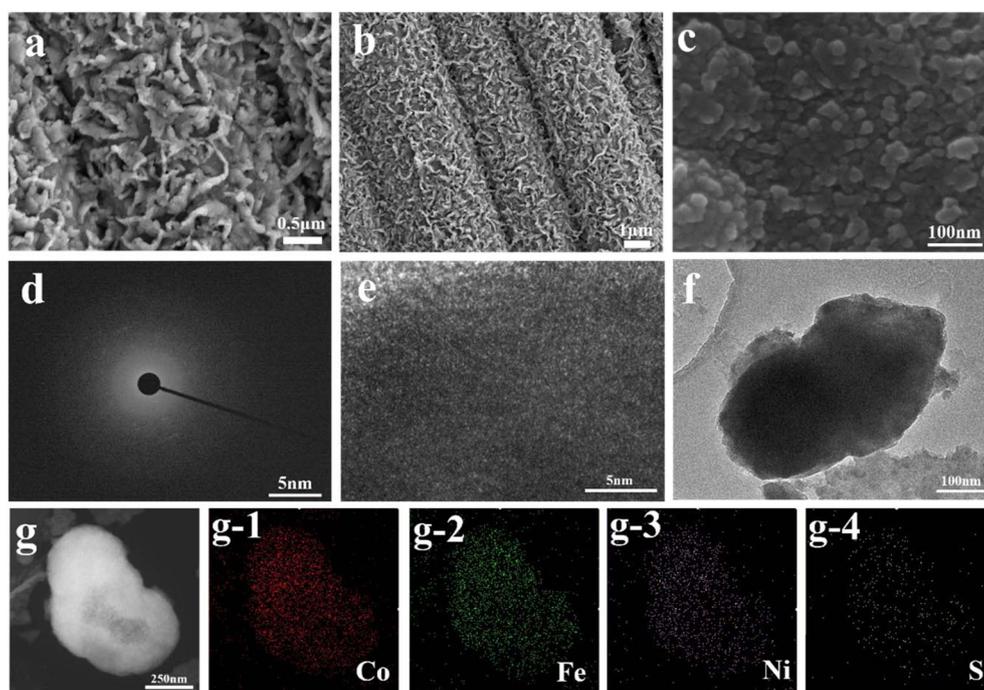

Fig. 1 The SEM images of (a and b) Co-Fe, (c) Co-Fe-Ni. (d) Selected-area electron diffraction (SAED), (e) HRTEM images, (f) TEM images of Co-Fe-Ni. (g–g4) Elemental distribution maps of Co, Fe, Ni and S in the Co-Fe-Ni.
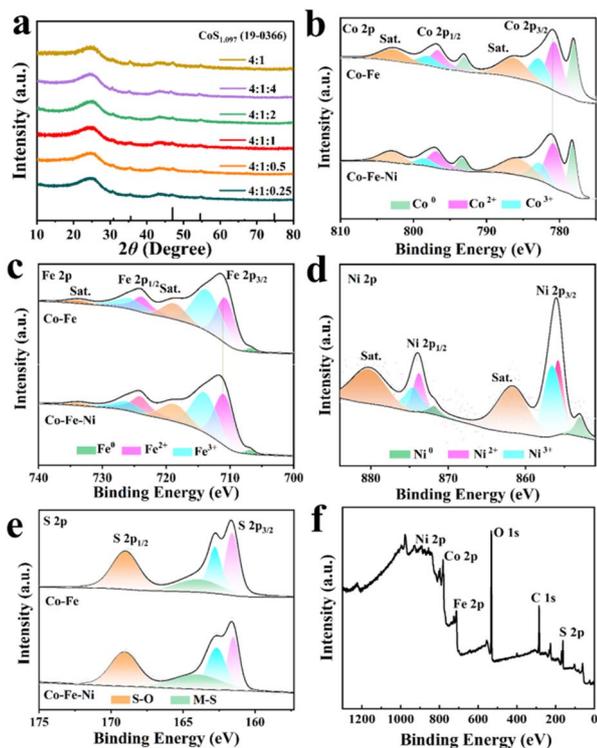
Fig. 2 (a) XRD patterns of Co-Fe and Co-Fe-Ni. (b) Co 2p spectra, (c) Fe 2p spectra, (d) Ni 2p spectra, (e) S 2p spectra of Co-Fe and Co-Fe-Ni. (f) Fully scanned XPS spectra of the Co-Fe-Ni sample.
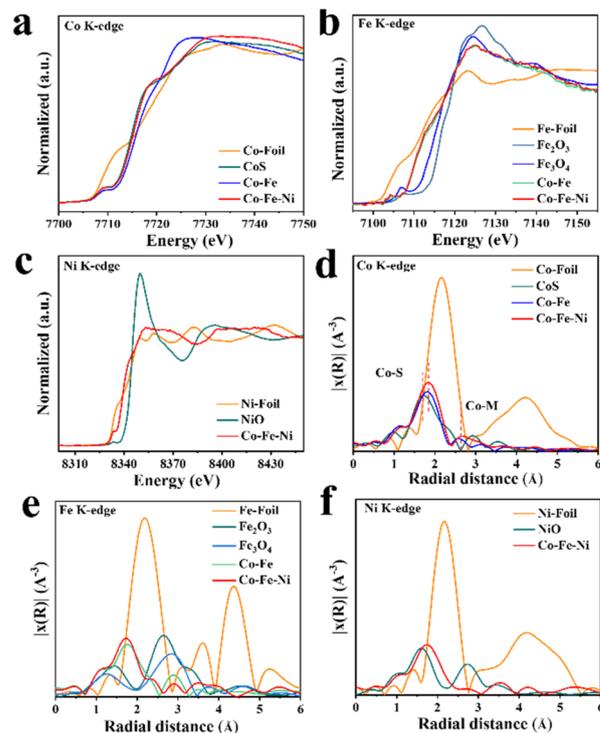

Fig. 3 XANES spectra at the (a) Co K-edge, (b) Fe K-edge and (c) Ni K-edge of the Co-Fe-Ni sample. (d) The corresponding FT K-edge EXAFS spectra of (d) Co, (e) Fe, and (f) Ni.

Co increases. Correspondingly, the Co 2p and Fe 2p XPS peaks shift slightly toward higher binding energies (Fig. 2b and c). This shift indicates a decrease in the electron cloud density around the Co and Fe atoms. The underlying reason can be attributed to the electronegativity difference between Ni and Co/Fe. Ni, with its higher electronegativity, exhibits a stronger ability to attract electrons, leading to a partial electron transfer from Co and Fe atoms to Ni. Fig. 2e shows the high-resolution S 2p spectra of Co-Fe-Ni, where the peaks at 161.5 eV and 162.6 eV correspond to S $2p_{3/2}$ and S $2p_{1/2}$, respectively.[55] Finally, the XPS survey spectrum (Fig. 2f) and SEM-EDS mappings (Fig. S5) confirms the simultaneous presence of Fe, Co, Ni, and S elements in the sample.

X-ray absorption spectroscopy (XAS) was performed to obtain detailed information about the coordination surroundings and the chemical valences of the Fe, Co, and Ni. The X-ray absorption near-edge structure (XANES) spectra of the samples, along with the corresponding references at the K-edge are presented in Fig. 3a, b and c. Fig. 3d, e and f display the k3-weighted Fourier transform (FT) extended X-ray absorption fine structure (EXAFS) spectra for the three samples. In Fig. 3a, the Co XANES spectra at the K-edge shows that, compared to Co foil and CoS, the Co absorption edge in Co-Fe and Co-Fe-Ni shifts gradually to the higher energy side, indicating that some electrons are transferred from Co to the Fe or Ni substitution. In the FT Co K-edge EXAFS (Fig. 3d), the peaks of Co-S bond for Co-Fe and Co-Fe-Ni are similar to the CoS sample, indicating the formation of Co-Fe-Ni. Fig. 3b reveals that the absorption edges

for Co-Fe and Co-Fe-Ni are situated between those of Fe foil and Fe_3O_4, suggesting that the valence state of Fe in Co-Fe and Co-Fe-Ni is between zero valence and trivalence. The EXAFS spectra of Co-Fe and Co-Fe-Ni show Fe-S bonds at 1.77 Å and 1.71 Å. The Ni K-edge XANES spectrum in Fig. 3c reveal that upon the introduction of Fe, the adsorption peak near the Ni edge exhibits a positive shift. These findings suggest that, consistent with previous literature reports, Fe can trigger the valence state transition of Ni.[56] In the FT Ni K-edge EXAFS spectrum of Co-Fe-Ni (Fig. 3f), the peaks located at 1.74 Å correspond to bond.[57] EXAFS fitting provided the coordination numbers of Co-S, Fe-S, and Ni-S (4.2, 3.8, and 4.0, respectively) and bond lengths (2.21 Å, 2.18 Å, and 2.23 Å, respectively). It was found that the introduction of Ni shortened the Co-S bond length by 0.05 Å, confirming electron transfer from Co to Ni and the formation of stronger metal-sulfur interactions. These results confirm the formation of Co-Fe-Ni compounds.

The electrochemical properties of the CoS, Co-Fe, and Co-Fe-Ni electrodes were systematically characterized. As illustrated in Fig. 4a–d, CV curves of CoS, Co-Fe, Co-Fe-Ni, and CC anode materials were measured with scan rates of 20–100 mV s^{-1} in PBS solution. The potential range is from −0.4 V to −0.3 V. From the data in Fig. 4e, the double-layer capacitance (C_{dl}) of each electrode stemmed from the equation of $C_{dl} = I/\nu$. The C_{dl} values for CoS, Co-Fe, Co-Fe-Ni, and CC were 5.4, 5.3, 6.37, and 1.06 mF cm^{-2}, respectively. The C_{dl} values of CoS, Co-Fe, and Co-Fe-Ni are approximately six times greater than that of CC. A larger electroactive surface area is crucial for improving MFC
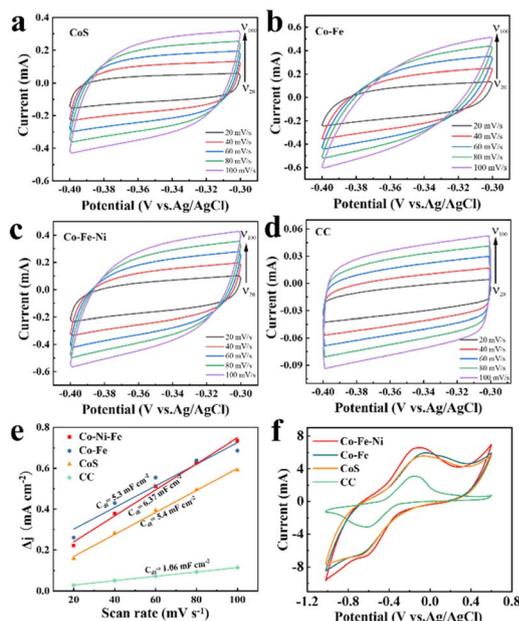
Fig. 4 CV measurements in PBS solution for (a) CoS, (b) Co-Fe, (c) Co-Fe-Ni, (d) CC. (e) The C_{dl} values of different electrodes are calculated by plotting the relationship between the scan rate and the corresponding average capacitance current. (f) CV curves were obtained for different anodes in an anolyte supplemented with *E. coli*.
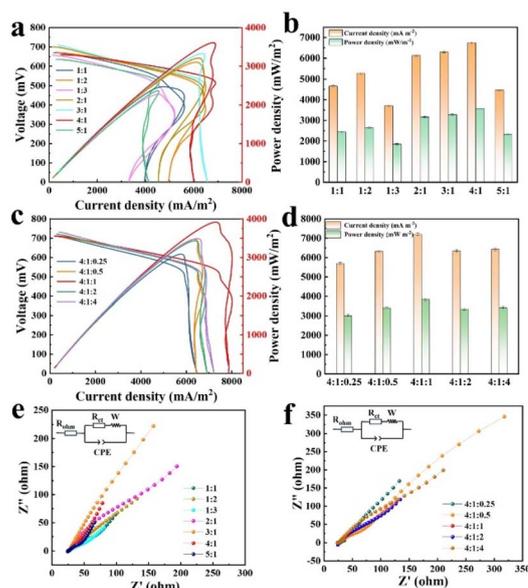

Fig. 5 (a) and (b) The power density curves and corresponding histograms with error bars for MFCs equipped with anodes of varying Co/Fe ratios. (c) and (d) The power density curves and corresponding histograms with error bars for MFCs equipped with anodes of varying Co/Fe/Ni ratios. (e) The EIS of different Co/Fe element ratios anode MFCs; (f) the EIS of different Co/Fe/Ni element ratios anode MFCs.

performance by providing more sites for electrochemical reactions, thus enhancing electron transfer and overall power output and efficiency. As shown in Table S1, the electrochemical active surface area (ECSA) of Co-Fe-Ni anode showing the highest ECSA. The cyclic voltammetry (CV) curves of CoS, Co-Fe, Co-Fe-Ni, and CC anodes was also conducted in the anolyte containing *E. coli*. with a rate of 100 mV s^{-1}, the potential range is between −1.0 V and 0.6 V. As shown in Fig. 4f, the peak redox currents of the CoS, Co-Fe, and Co-Fe-Ni anodes were greater than those of the CC anode, demonstrating enhanced electron transfer efficiency between the active microorganisms and the CoS, Co-Fe, and Co-Fe-Ni anodes. This also suggests that the CoS, Co-Fe, and Co-Fe-Ni anodes have larger active surface areas compared to the CC anode.

During MFCs operation, three independent replicate reactors equipped with identical anode materials were tested for each experimental group. After an initial operating period, the output voltages stabilized. Considering the influence of scan rate on power density measurements, the power density profiles of MFCs with Co-Fe and Co-Fe-Ni anodes were specifically examined with a rate of 1 mV s^{-1}. Following optimization of the Co/Fe ratio, the MFCs achieved a maximum power density of 3611 ± 104 mW m^{-2} and a maximum current density of 6801 mA m^{-2} at a Co/Fe ratio of 4 : 1 (Fig. 5a and b).

To further enhance the power density of MFCs, different proportions of Ni were doped into Co-Fe, with Co/Fe/Ni ratios of 4 : 1 : 0.25, 4 : 1 : 0.5, 4 : 1 : 1, 4 : 1 : 2, and 4 : 1 : 4. The corresponding power densities were 3085, 3472, 3915, 3433, and 3488 mW m^{-2}, respectively. The Co-Fe-Ni anode material significantly improved both the current and power densities of the

MFCs, with the maximum the current density reaching 7290 ± 210 mA m^{-2} and power density reaching 3915 ± 78 mW m^{-2} (Fig. 5c and d). Statistical analysis (Student's *t*-test, *t*-test, $t \approx 4.606$, $df \approx 3.71$, $p = 0.017$, $n = 3$) confirms that this represents a significant increase of 8.4% in power density compared to the Co-Fe anode without Ni. The enhanced performance is attributed to the combined effects of the multi-element composition, which modulates the charge state and significantly improves the catalytic activity of the metal sulfides.[44] As shown in Fig. S6, under identical measurement conditions, the bare carbon cloth yields significantly lower current and power output. This direct comparison validates that the electrodeposited Co-Fe-Ni sulfide layer is primarily responsible for the enhanced electrocatalytic activity. As shown in the EIS spectra of Co-Fe anodes with different Co/Fe ratios (Fig. 5e), the composition significantly influences the charge transfer resistance (R_{ct}). The fitting results (Table S2) indicate that the Co/Fe (4 : 1) anode exhibits the smallest R_{ct} value among the binary Co-Fe compositions. By establishing the Co/Fe (4 : 1) as the optimal binary host with the most favorable charge transfer characteristics, the subsequent introduction of Ni was strategically performed on this best-performing baseline. This allows us to attribute the further performance enhancement (to 3915 mW m^{-2}) specifically to the synergistic effects of Ni, rather than to a suboptimal Co/Fe ratio. This optimal ratio likely strikes a balance between creating sufficient catalytically active sites and maintaining good electrical conductivity. The lower R_{ct} facilitates more efficient electron transfer from the electrogenic bacteria to the anode, which is a key factor contributing to its superior power density (3611 mW m^{-2}, as shown in Fig. 5a) compared to other Co/Fe ratios.
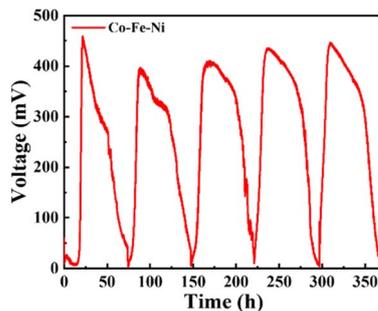
Fig. 6 Five consecutive discharge cycles of MFCs with a Co-Fe-Ni (4 : 1 : 1) anode.

This optimization of the binary Co-Fe system provided an ideal baseline and a structurally favorable host for the subsequent introduction of Ni. The goal of Ni doping was to further modulate the electronic structure and enhance the electrocatalytic properties of this already optimized binary foundation.

Fig. 6 presents five constant-resistance discharge cycles of the MFC voltage output using a Co-Fe-Ni alloy anode. All discharge cycles were performed under consistent operational conditions: a temperature of 37 °C, an external load of 1000 Ω, and an anaerobic environment in the anode chamber. After each cycle, the anolyte and catholyte were refreshed (replenishing glucose, yeast extract, *E. coli* and HNQ to initial concentrations) to avoid nutrient depletion, while the cathode electrolyte and electrode materials remained unchanged. The results demonstrate excellent stability of the anode after five cycles, with the maximum voltage maintaining 0.4–0.5 V without significant decay. The SEM images of the Co-Fe-Ni alloy anode after stability testing reveals that the nanoparticle morphology remains well-preserved (Fig. S7a and b). There is no obvious detachment, or falling off observed on the carbon cloth substrate. This indicates robust mechanical adhesion and morphological integrity of the catalyst lead to the outstanding stability. This long-term durability highlights the potential of Co-Fe-Ni nanomaterials for practical applications in MFCs. Bacterial freeze-drying fixation of the electrodes after anodic operation revealed a higher bacterial cell density on the surface of the Co-Fe-Ni anode compared to that of the Co-Fe anode (Fig. S8). This difference in biofilm colonization is one of the factors contributing to the superior performance of MFCs equipped with Co-Fe-Ni anodes over those using Co-Fe anodes.

Table S4 compares the power densities of MFCs using *E. coli* and other microorganisms. The results clearly show that MFCs with a Co-Fe-Ni anode deliver a higher power density than those reported in earlier studies. In general, the morphology and composition play a crucial role in governing the current and power densities of Co-Fe-Ni-based MFCs. Specifically, the current and power densities are remarkably higher with Ni doping compared to the case without Ni.

4.   Conclusion

In this study, a ternary transition metal Co-Fe-Ni sulfide was synthesized *via* a one-step solvothermal method. By tuning the molar ratios of Co, Fe, and Ni precursors, the performance of microbial fuel cells (MFCs) was significantly enhanced, achieving a maximum power density of 3915 mW m^{-2}. The synergistic interaction among Co, Fe, and Ni elements led to an approximately 8.4% increase in power density compared to Co-Fe-based MFCs. This improvement is attributed to the incorporation of Ni, which effectively reduced the internal impedance of the MFCs, facilitated electron transfer at the anode interface, and promoted microbial metabolic activity. Consequently, the overall electrical energy output was markedly improved, demonstrating a promising strategy for optimizing energy recovery from wastewater.

Author contributions

Qilin Guo: writing – original draft, investigation, formal analysis. Jianchun Ma: formal analysis. Wenbo Lu: formal analysis. Ying Wang: formal analysis. Ergui Luo: investigation. He Xiao: data curation. Li Zhang: data curation. Haishun Wu: software, formal analysis. Tianjun Hu: project administration, conceptualization, investigation. Jianfeng Jia: writing – review & editing, supervision.

Conflicts of interest

The authors declare that they have no known competing financial interests or personal relationships that could have appeared to influence the work reported in this paper.

Data availability

The data supporting this article have been included as part of the supplementary information (SI). Supplementary information: morphological and structural characterization of some control samples, as well as data fitting results. See DOI: https://doi.org/10.1039/d5ra08874g.

Acknowledgements

References

1 D. Guo, H.-F. Wei, X.-Y. Yu, Q. Xia, Z. Chen, J.-R. Zhang, R.-B. Song and J.-J. Zhu, *Nano Energy*, 2019, **57**, 94–100.

2 A. Sharma, P. Sarkar, M. Chhabra, A. Kumar, A. Kumar, H. Kothadia and A. Mallick, *Chem. Eng. J.*, 2023, **476**, 146578.

3 M. Jian, P. Xue, K. Shi, R. Li, L. Ma and P. Li, *J. Hazard. Mater.*, 2020, **388**, 122123.

4 Y. Yoon, B. Kim and M. Cho, *Water Res.*, 2023, **244**, 120482.

5 I. M. R. Fattah, J. Alom, J. U. Zaman, S. Ban, I. Veza, M. A. Kalam, V. Hessel and M. B. Ahmed, *J. Power Sources*, 2025, **625**, 235688.

6 J. Ma, N. Shi, Y. Zhang, J. Zhang, T. Hu, H. Xiao, T. Tang and J. Jia, *J. Power Sources*, 2020, **450**, 227628.

7 P. D. Kolubah, H. O. Mohamed, M. Ayach, A. Rao Hari, H. N. Alshareef, P. Saikaly, K.-J. Chae and P. Castaño, *Chem. Eng. J.*, 2023, **461**, 141821.

8 S. A. Erenler, T. Unver, B. F. Ozaslan, S. Koytepe and S. Sezer, *Fuel*, 2024, **363**, 130976.

9 R. S. Chouhan, S. Gandhi, S. K. Verma, I. Jerman, S. Baker and M. Štrok, *Renewable Sustainable Energy Rev.*, 2023, **188**, 113813.

10 J. Li and Z. Chen, *Chem. Eng. J.*, 2024, **489**, 151323.

11 D. Wang, Z. Ma, Y. E. Xie and H. Song, *J. Energy Chem.*, 2017, **26**, 1187–1195.

12 L. He, P. Du, Y. Chen, H. Lu, X. Cheng, B. Chang and Z. Wang, *Renewable Sustainable Energy Rev.*, 2017, **71**, 388–403.

13 E. Tian, Y. Liu, X. Wang, L. Fang, L. Zheng, C. Song, S. Lu and H. Liu, *Chem. Eng. J.*, 2024, **489**, 151284.

14 B. Yu, L. Feng, Y. He, L. Yang and Y. Xun, *J. Hazard. Mater.*, 2021, **401**, 123394.

15 C.-e. Zhao, P. Gai, R. Song, Y. Chen, J. Zhang and J.-J. Zhu, *Chem. Soc. Rev.*, 2017, **46**, 1545–1564.

16 R. Wang, M. Yan, H. Li, L. Zhang, B. Peng, J. Sun, D. Liu and S. Liu, *Adv. Mater.*, 2018, **30**, 1800618.

17 A. Godain, T. M. Vogel, P. Fongarland and N. Haddour, *Biosens. Bioelectron.*, 2024, **244**, 115806.

18 L. Chen, P. Zhang, W. Shang, H. Zhang, Y. Li, W. Zhang, Z. Zhang and F. Liu, *Bioelectrochemistry*, 2018, **121**, 65–73.

19 N. N. Mohd Noor, N. I. Oktavitri and K. Kim, *Fuel*, 2024, **367**, 131438.

20 M. Kamali, Y. Guo, T. M. Aminabhavi, R. Abbassi, R. Dewil and L. Appels, *Renewable Sustainable Energy Rev.*, 2023, **173**, 113095.

21 E. Tian, Y. Liu, F. Yin, S. Lu, L. Zheng, X. Wang, Z. Wang and H. Liu, *Chem. Eng. J.*, 2023, **451**, 138767.

22 A. J. Slate, K. A. Whitehead, D. A. C. Brownson and C. E. Banks, *Renewable Sustainable Energy Rev.*, 2019, **101**, 60–81.

23 B. Kim, S. V. Mohan, D. Fapyane and I. S. Chang, *Trends Biotechnol.*, 2020, **38**, 667–678.

24 L. Zhang, R. Wang, H. Li, J. Sun, M. Li, Y. Qiu and S. Liu, *Chem. Eng. J.*, 2024, **500**, 156807.

25 F. Li, D. Wang, Q. Liu, B. Wang, W. Zhong, M. Li, K. Liu, Z. Lu, H. Jiang, Q. Zhao and C. Xiong, *J. Power Sources*, 2019, **412**, 514–519.

26 Y. Yin, G. Huang, Y. Tong, Y. Liu and L. Zhang, *J. Power Sources*, 2013, **237**, 58–63.

27 Z. Al-Qodah, M. Al-Shannag, M. Al-Busoul, I. Penchev and W. Orfali, *Biochem. Eng. J.*, 2017, **121**, 94–106.

28 E. Katz, O. Lioubashevski and I. Willner, *J. Am. Chem. Soc.*, 2005, **127**, 3979–3988.

29 W.-W. Li, G.-P. Sheng, X.-W. Liu, P.-J. Cai, M. Sun, X. Xiao, Y.-K. Wang, Z.-H. Tong, F. Dong and H.-Q. Yu, *Biosens. Bioelectron.*, 2011, **26**, 3987–3992.

30 L. Chen, Y. Li, J. Yao, G. Wu, B. Yang, L. Lei, Y. Hou and Z. Li, *J. Power Sources*, 2019, **412**, 86–92.

31 S. Narayanasamy and J. Jayaprakash, *Chem. Eng. J.*, 2018, **343**, 258–269.

32 C. Ren, K. Li, C. Lv, Y. Zhao, J. Wang and S. Guo, *J. Electroanal. Chem.*, 2019, **840**, 134–143.

33 Z. Wang, P. Fei, H. Xiong, C. Qin, W. Zhao and X. Liu, *Electrochim. Acta*, 2017, **252**, 295–305.

34 S. Jin, Y. Feng, J. Jia, F. Zhao, Z. Wu, P. Long, F. Li, H. Yu, C. Yang, Q. Liu, B. Zhang, H. Song and W. Feng, *Energy Environ. Mater.*, 2023, **6**, e12373.

35 H. Tang, Y. Zeng, Y. Zeng, R. Wang, S. Cai, C. Liao, H. Cai, X. Lu and P. Tsiakaras, *Appl. Catal., B*, 2017, **202**, 550–556.

36 L. Zhou, C. Yang, J. Wen, P. Fu, Y. Zhang, J. Sun, H. Wang and Y. Yuan, *J. Mater. Chem. A*, 2017, **5**, 19343–19350.

37 T. Ren, Y. Liu, X. Lin and C. Li, *J. Mater. Chem. A*, 2024, **12**, 8447–8456.

38 M. Yu, X. Cheng, Y. Zeng, Z. Wang, Y. Tong, X. Lu and S. Yang, *Angew. Chem., Int. Ed.*, 2016, **55**, 6762–6766.

39 Y. Liu, J. Wang, Y. Sun, H. Li, Z. Zhai, S. Guo, T. Ren and C. Li, *J. Power Sources*, 2022, **544**, 231890.

40 J. M. Veglak, A. Tsai, S. S. Soliman, G. R. Dey and R. E. Schaak, *J. Am. Chem. Soc.*, 2024, **146**, 19521–19536.

41 C. R. McCormick and R. E. Schaak, *J. Am. Chem. Soc.*, 2021, **143**, 1017–1023.

42 X. Du, J. Huang, J. Zhang, Y. Yan, C. Wu, Y. Hu, C. Yan, T. Lei, W. Chen, C. Fan and J. Xiong, *Angew. Chem., Int. Ed.*, 2019, **58**, 4484–4502.

43 Z. W. Seh, J. Kibsgaard, C. F. Dickens, I. Chorkendorff, J. K. Nørskov and T. F. Jaramillo, *Science*, 2017, **355**, 4998.

44 L. Wu, X. Shen, Z. Ji, J. Yuan, S. Yang, G. Zhu, L. Chen, L. Kong and H. Zhou, *Adv. Funct. Mater.*, 2023, **33**, 2208170.

45 T. Wu, Y. Sun, X. Ren, J. Wang, J. Song, Y. Pan, Y. Mu, J. Zhang, Q. Cheng, G. Xian, S. Xi, C. Shen, H.-J. Gao, A. C. Fisher, M. P. Sherburne, Y. Du, J. W. Ager, J. Gracia, H. Yang, L. Zeng and Z. J. Xu, *Adv. Mater.*, 2023, **35**, 2207041.

46 J. Jiang, C. Yan, X. Zhao, H. Luo, Z. Xue and T. Mu, *Green Chem.*, 2017, **19**, 3023–3031.

47 G. Li, Y. Tang, T. Fu, Y. Xiang, Z. Xiong, Y. Si, C. Guo and Z. Jiang, *Chem. Eng. J.*, 2022, **429**, 132174.

48 Q. Guo, J. Ma, T. Hu, Y. Wang, W. Lu, J. Zhang, E. Luo, H. Xiao, M. Zhao, L. Zhang and J. Jia, *Biosens. Bioelectron.*, 2026, **292**, 118091.

49 Y. Ojima, T. Kawaguchi, S. Fukui, R. Kikuchi, K. Terao, D. Koma, T. Ohmoto and M. Azuma, *Bioprocess Biosyst. Eng.*, 2020, **43**, 323–332.

50 J. Ma, N. Shi and J. Jia, *Electrochim. Acta*, 2020, **362**, 137126.

51 Y. Yue, X. Zou, Y. Shi, J. Cai, Y. Xiang, Z. Li and S. Lin, *J. Electroanal. Chem.*, 2023, **928**, 117089.

52 H. O. Mohamed, M. Obaid, A. S. Yasin, J. H. Kim and N. A. Barakat, *RSC Adv.*, 2016, **6**, 111657–111665.

53 N. Gao, Y. Zhang, C. Chen, B. Li, W. Li, H. Lu, L. Yu, S. Zheng and B. Wang, *J. Mater. Chem. A*, 2022, **10**, 8378–8389.

54 Y. Li, Z. Zhu, Y. L. Zhong, Y. Jin, P. Saha and Q. Cheng, *J. Power Sources*, 2024, **614**, 234969.

55 L. Wang, Y. Yan, R. Li, X. Han, J. Li, T. Ran, J. Li, B. Xiong, X. Song, Z. Yin, H. Wang, Q. Zhu, B. Cheng and Z. Yin, *Chin. Chem. Lett.*, 2024, **35**, 110011.

56 M. Görlin, P. Chernev, J. Ferreira de Araújo, T. Reier, S. Dresp, B. Paul, R. Krähnert, H. Dau and P. Strasser, *J. Am. Chem. Soc.*, 2016, **138**, 5603–5614.

57 Z. Gu, Y. Zhang, X. Wei, Z. Duan, L. Ren, J. Ji, X. Zhang, Y. Zhang, Q. Gong, H. Wu and K. Luo, *Adv. Sci.*, 2022, **9**, 2201903.